Anisotropic damping and wave vector dependent susceptibility of the spin fluctuations in $La_{2-x}Sr_xCuO_4$ studied by resonant inelastic x-ray scattering

H. C. Robarts,[1,2] M. Barthélemy,[1] K. Kummer,[3] M. García-Fernández,[2] J. Li,[2,4] A. Nag,[2] A. C. Walters,[2] K. J. Zhou,[2,*] and S. M. Hayden[1,†]

[1]*H. H. Wills Physics Laboratory, University of Bristol, Bristol BS8 1TL, United Kingdom*

[2]*Diamond Light Source, Harwell Science & Innovation Campus, Didcot, Oxfordshire OX11 0DE, United Kingdom*

[3]*European Synchrotron Radiation Facility, 71 Avenue des Martyrs, 38000 Grenoble, France*

[4]*Beijing National Laboratory for Condensed Matter Physics and Institute of Physics, Chinese Academy of Sciences, Beijing 100190, China*

(Received 8 August 2019; revised manuscript received 30 October 2019; published 19 December 2019)

We report high-resolution resonant inelastic x-ray scattering (RIXS) measurements of the collective spin fluctuations in three compositions of the superconducting cuprate system $La_{2-x}Sr_xCuO_4$. We have mapped out the excitations throughout much of the two-dimensional (h, k) Brillouin zone. The spin fluctuations in $La_{2-x}Sr_xCuO_4$ are found to be fairly well described by a damped harmonic oscillator model, thus our data allows us to determine the full wave vector dependence of the damping parameter. This parameter increases with doping and is largest along the (h, h) line, where it is peaked near (0.2, 0.2). We have used a new procedure to determine the absolute wave vector dependent susceptibility for the doped compositions $La_{2-x}Sr_xCuO_4$ ($x = 0.12, 0.16$) by normalizing our data to La_2CuO_4 measurements made with inelastic neutron scattering (INS). We find that the evolution with doping of the intensity of high-energy excitations measured by RIXS and INS is consistent. For the doped compositions, the wave vector dependent susceptibility is much larger at $(\frac{1}{4}, \frac{1}{4})$ than at $(\frac{1}{2}, 0)$. It increases rapidly along the (h, h) line towards the antiferromagnetic wave vector of the parent compound $(\frac{1}{2}, \frac{1}{2})$. Thus, the strongest magnetic excitations, and those predicted to favor superconductive pairing, occur towards the $(\frac{1}{2}, \frac{1}{2})$ position as observed by INS.

DOI: 10.1103/PhysRevB.100.214510

I. INTRODUCTION

The origin of high temperature superconductivity (HTS) in doped layered cuprate materials remains a subject of intense interest in both experimental and theoretical research, despite over 30 years of activity. It is widely believed that the magnetic degrees of freedom and in particular spin fluctuations are primarily responsible for superconductive pairing in the cuprates [1–4]. In this case, it is important to characterize the collective spin excitations as a function of wave vector, energy, doping, and temperature to see how they correlate with the occurrence of superconductivity and compare with theoretical models.

Resonant inelastic x-ray scattering (RIXS) [5–14] and inelastic neutron scattering (INS) [15–21] are complementary probes which directly yield information about the wave vector and energy of the dynamical structure factor $S(\mathbf{Q}, \omega)$ or dynamic susceptibility (response function) $\chi''(\mathbf{Q}, \omega)$ at high frequencies. The $La_{2-x}Sr_xCuO_4$ (LSCO) system allows the evolution of $S(\mathbf{Q}, \omega)$ to be measured across the phase diagram, from the antiferromagnetic (AF) parent compound La_2CuO_4 (LCO) through superconducting compositions.

In La_2CuO_4, the spin waves have their lowest energies at the Γ, $\mathbf{Q} = (0, 0)$ and M, $\mathbf{Q} = (\frac{1}{2}, \frac{1}{2})$ positions and $\chi''(\mathbf{Q}, \omega)$ is small near Γ and largest near M. INS measurements [15,19,20] throughout the Brillouin zone have shown that the magnetic excitations can be fairly well described as spin waves derived from a Heisenberg model with next-nearest neighbor interactions including a ring exchange. As expected, they are strongest near the AF wave vector $\mathbf{Q} = (\frac{1}{2}, \frac{1}{2})$ and show anomalously strong damping at the X or $(\frac{1}{2}, 0)$ position [10,20,22].

For superconducting compositions in LSCO, INS shows that the strongest response [16,21,23–25] occurs near $\mathbf{Q} = (\frac{1}{2}, \frac{1}{2})$ at low and intermediate energies (0–150 meV), with comparable intensity to the parent antiferromagnet. For optimally doped ($x = 0.16$) LSCO, an incommensurate structure is observed [23] for $\hbar\omega \lesssim 25$ meV. Above 50 meV the magnetic excitations disperse [21,23,25] away from $(\frac{1}{2}, \frac{1}{2})$. At high energies, $\hbar\omega \approx 250$ meV, excitations are observed [16] on the Brillouin zone boundary at $\mathbf{Q} = (\frac{1}{2}, 0)$ in LSCO ($x = 0.14$) demonstrating the persistence of high energy spin excitations for superconducting compositions. For overdoped compositions [21,24] $x = 0.22$–0.25, the lower energy ($\hbar\omega \sim 50$ meV) features observed at optimal doping are suppressed.

Cu L_3 RIXS [6,7,10–14,26] measurements of the spin fluctuation in LSCO are complementary to INS. They are restricted to a circular region in (h, k) centered on Γ [see Figs. 1(a) and 1(b)] but are able to isolate high energy excitations ($\hbar\omega \gtrsim 300$ meV) more easily. Early RIXS measurements in LSCO [7] verified the existence of dispersing spin fluctuations. Spin excitations are observed [7,11–14,26]

*kejin.zhou@diamond.ac.uk

†s.hayden@bristol.ac.uk

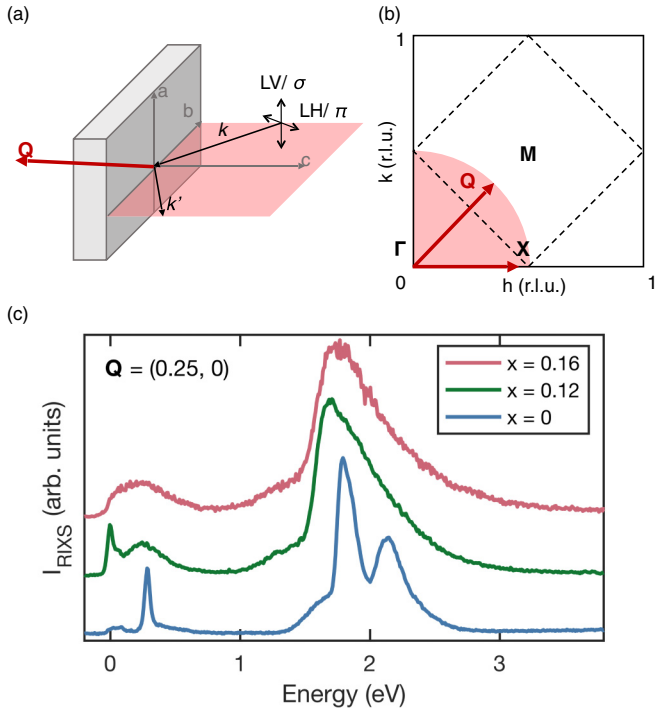

FIG. 1. Experimental geometry showing (a) the scattering plane in relation to the crystal axis and (b) the resulting measured region of the LSCO unit cell. The measured wave vectors $\mathbf{Q} = \mathbf{k} - \mathbf{k}'$ giving the measurement regions indicated in red. With our definitions, grazing out for $\mathbf{k}'$ corresponds to positive h and k. (c) Example RIXS spectra from each compound at $\mathbf{Q} = (0.25, 0)$.

throughout the first AF Brillouin zone including at the boundary [e.g., $(\frac{1}{2}, 0)$ position] where INS [16] also finds excitations. RIXS studies suggest that these excitations show wave vector dependent damping [11,13,26]. Spin fluctuations persist to overdoped compositions and evolve relatively slowly with doping [11,13].

The improved energy resolution of the measurements we have performed allows us to model the nature of the spin fluctuations more precisely. The motivation of this work is to perform a systematic characterization of the spin fluctuations in LSCO with this enhanced energy resolution including mapping the $\mathbf{Q}$ dependence of the frequency and damping throughout a two-dimensional (2D) portion of the Brillouin zone. We also aim to bridge the techniques of INS and RIXS to establish an estimate of the absolute spin susceptibility.

Here we report RIXS measurements on three dopings of LSCO, $x = 0$, 0.12, and 0.16. We have made use of the high resolution and high intensity of the RIXS spectrometers ID32 at the European Synchrotron Radiation Facility (ESRF) and I21 at the Diamond Light Source (DLS) to map out magnetic spectra over 2D (h, k) space. We find that, for doped compositions, the magnetic response is fairly well described by a damped harmonic oscillator line shape. The pole frequency and damping are strongly anisotropic in agreement with previous studies along the $(h, 0)$ [11] and (h, h) [26] lines, with the strongest damping along the (h, h) line and centered near (0.2, 0.2) for the optimally doped composition. By comparing data on La_2CuO_4, where the spin waves are well studied, with LSCO, we make quantitative estimates of the wave vector dependent susceptibility $\chi'(\mathbf{Q})$. This quantity is a vital input to theories of the HTS phenomenon [1–3].

II. EXPERIMENTAL DETAILS

A. Samples

Measurements were performed on single crystal samples of LSCO. Three different compositions were measured: the $x = 0$ parent compound which displays antiferromagnetism below $T_N \simeq 320$ K [20] and two hole-doped compounds [23,27], $x = 0.12 \pm 0.005$ ($T_c = 29.5$ K), and $x = 0.16 \pm 0.005$ ($T_c = 38$ K). The $x = 0.16$ composition is close to optimal doping for the superconducting phase and $x = 0.12$ shows charge density wave (CDW) order with short range CDW correlations developing at $T \sim 150$ K and a longer range CDW developing at $T_{\mathrm{CDW}} \simeq 75$ K [27]. Crystals were grown via the traveling solvent floating zone technique and used in previous neutron [20,21,23] and x-ray [27] studies. The crystals were recut into posts with typical dimensions $\simeq 2 \times 1 \times 1\,\mathrm{mm}^3$. The samples were aligned using Laue x-ray diffraction and cleaved *in situ* to expose a clean surface to the beam. The sample used for measurements of the $x = 0.12$ compound at the ESRF was polished following the procedure in Croft *et al.* [27]. For the same composition, the elastic peak observed close to the specular condition is approximately 15 times greater in the polished sample compared to the cleaved sample. This makes the low energy excitations at low $\mathbf{Q}$ difficult to extract and we therefore only use data from this sample in the map plots. We verified that the line shape, intensity, and energy of the magnetic excitations is the same in both data sets.

B. Notation

LSCO undergoes a structural transition to a low-temperature orthorhombic (LTO) phase below $T_{\mathrm{LTO}} \simeq 240$ K, however, we use the high-temperature tetragonal (HTT) $I/4mmm$ crystal structure notation to allow comparison between the three compounds. In this notation, $a = b \simeq 3.8$ Å, $c \simeq 13.2$ Å. The momentum transfer $\mathbf{Q}$ is defined in reciprocal lattice units (r.l.u.) as $\mathbf{Q} = h\mathbf{a}^* + k\mathbf{b}^* + l\mathbf{c}^*$ where $\mathbf{a}^* = 2\pi/a$, etc. The measured excitations are labeled via their energies $\hbar\omega = c|\mathbf{k}| - c|\mathbf{k}'|$ and momenta $\mathbf{Q} = \mathbf{k} - \mathbf{k}'$, where $\mathbf{k}$ and $\mathbf{k}'$ are in initial and final wave vectors.

C. Spectrometers

High resolution RIXS spectra were measured at beamline ID32 of the ESRF [28,29] and the I21 RIXS spectrometer at DLS [30]. The incoming beam energy was tuned to the Cu L_3 edge (~932 eV) with linear horizontal (LH) π polarization. We present LH data from the grazing-out orientation where the single magnon intensity is favored [31,32]. Recent experiments with polarization analysis [33,34] have established that this configuration is primarily sensitive to magnetic scattering. Samples were mounted on the sample holder in ultrahigh vacuum and cooled to $T \simeq 20$ K. Magnetic excitations in cuprates are dispersive predominantly in the a-b plane of LSCO, allowing paths to be measured in the (h, k) plane by varying the sample orientation, and keeping the scattering

angle 2θ fixed at 146° and 149.5° for I21 and ID32, respectively. The scattering geometry is shown in Fig. 1(a). We assume there is negligible dispersion in the features of interest from variation of l, and therefore we focus only on the momentum transferred in the (h, k) plane. Spectra were principally measured along the two high-symmetry lines $(h, 0)$ and (h, h) as indicated with red arrows in Fig. 1(b) with energy resolution $\Delta E \simeq 35$ meV. The $x = 0$ and 0.12 measurements were performed at I21 and the $x = 0.16$ measurements were performed at ID32 and repeated at I21. In both doped compounds, further measurements were performed at ID32 with $\Delta E \simeq 50$ meV on a grid of $\mathbf{Q}$ points evenly distributed throughout a quadrant of the Brillouin zone indicated by the red shaded region in Fig. 1(b). The energy resolution was established using elastic scattering from a silver paint or carbon tape reference. For I21, a background was measured from either a dark image taken after the collection or by fitting a constant background outside the excitation range $\leqslant -0.1$ and $\geqslant 5$ eV.

D. Analysis

1. Data processing

In order to carry out a quantitative analysis of the data, we follow recent practice [6,7,13,26,33,35] and assume that the magnetic intensity observed in RIXS is proportional to the spin-spin dynamical structure factor $S(\mathbf{Q}, \omega)$ which is used to interpret neutron scattering experiments [36]. $S(\mathbf{Q}, \omega)$ is, in turn, proportional to $\chi''(\mathbf{Q}, \omega)$ multiplied by the Bose factor $n(\omega) + 1 = [1 - \exp(-\hbar\omega/k_B T)]^{-1}$. Clearly the scattering processes in RIXS and INS are very different, with the observed RIXS intensity being dependent on the relative orientation of the photon electric field to the Cu $3d$ orbitals as well as the absorption of the x-ray photons within the sample. These factors are known to vary slowly with $\mathbf{Q}$ [37,38], nevertheless, to correct for these effects we initially normalize our raw counts I_{raw} to the energy-integrated dd excitation intensity obtained from the same spectrum. The intensity of the dd excitations is known to be dependent on the polarization ϵ and wave vector $\mathbf{k}$ and can be described by a function $g(\epsilon, \epsilon', \mathbf{k}, \mathbf{k}')$. We denote the measured intensity I_{RIXS} as I_{raw}/g where $g = \int g(\epsilon, \epsilon', \mathbf{k}, \mathbf{k}')\, d\omega$ is the integral described above evaluated over the range 1–3 eV.

The spectra were aligned to the elastic reference and the exact zero-energy position was established by fitting an elastic peak with a Gaussian function. The aligned spectra were modeled within a range −80 to 800 meV. As well as the spin excitations, we fit an elastic peak and low-energy excitations, which are interpreted as phonons, using Gaussian functions. Electron-hole excitations and broadened dd excitations contribute to the low-energy RIXS scattering for doped compositions [11]. This contribution was modeled with a linear function which was fixed for all spectra of the same composition. The gradient of the linear function was found by fitting the spectra at low $\mathbf{Q}$. In the insulating parent compound this contribution was not required. However, a broad continuum of multimagnon excitations is resolvable at ∼400−600 meV. This was modeled with a Gaussian function.

The spectra were not deconvolved to take account of the instrument energy resolution ≃35 meV. The most noticeable effect of this was in the determination of γ and Γ values (see Sec. II D 2). We estimate that our fitted values are increased by 5% in the worse case.

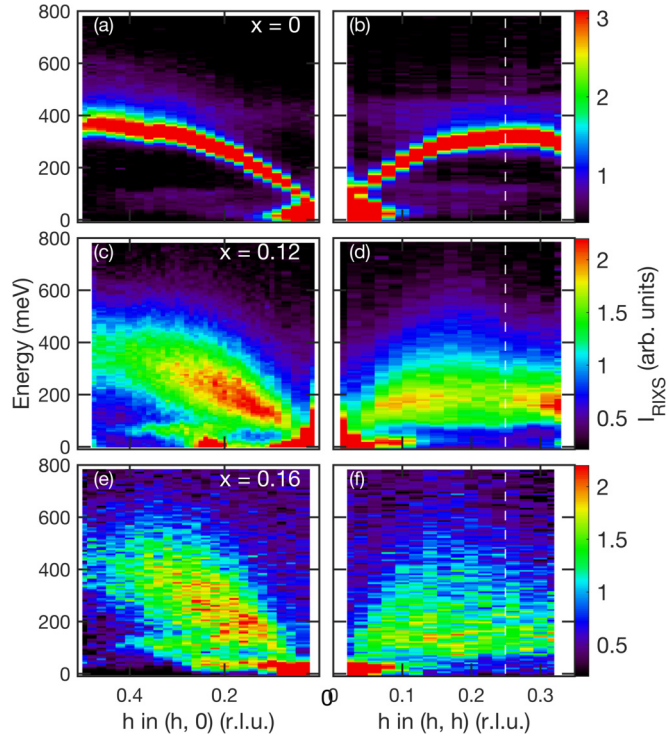

FIG. 2. I_{RIXS} intensity maps as a function of $\mathbf{Q}$ in LSCO $x = 0$ ($T \approx 20$ K), 0.12, and 0.16 ($T \approx 30$ K). Showing measurements along the $(h, 0)$ and (h, h) lines. The measurements were performed in grazing-out geometry and with LH polarization at I21 at Diamond Light Source. The configuration favors magnetic scattering. All three compositions show charge scattering in the form of phonons below 100 meV and a charge density wave peak is observed near $h = 0.23$ in $x = 0.12$. The dashed white line marks the antiferromagnetic Brillouin zone boundary (see Fig. 1).

2. Damped harmonic oscillator model

A damped harmonic oscillator (DHO) model may be used to describe a given spin-wave mode with wave vector $\mathbf{Q}$. This approach has recently been taken in a number of RIXS studies [11,13,33,39]. The analogous mechanical DHO equation is [40]

$$\ddot{x} + \omega_0^2 x + \gamma \dot{x} = f/m, \tag{1}$$

where ω_0 is the frequency of the undamped mode and γ is the damping parameter. In our case, both of these are $\mathbf{Q}$ dependent, thus $\omega_0 = \omega_0(\mathbf{Q})$ and $\gamma = \gamma(\mathbf{Q})$.

The imaginary part of the DHO response function for a given wave vector can be written as

$$\chi''(\mathbf{Q}, \omega) = \frac{\chi'(\mathbf{Q})\, \omega_0^2(\mathbf{Q})\, \gamma(\mathbf{Q})\, \omega}{\left[\omega^2 - \omega_0^2(\mathbf{Q})\right]^2 + \omega^2 \gamma^2(\mathbf{Q})}, \tag{2}$$

where $\chi(\mathbf{Q}) \equiv \chi'(\mathbf{Q}) \equiv \chi'(\mathbf{Q}, \omega = 0)$ is the real part of the zero frequency susceptibility. The solution of Eq. (1) can be represented by two poles with complex frequencies:

$$\omega = \pm\left[\omega_0^2 - \left(\gamma^2/4\right)\right]^{1/2} = \pm\omega_1 - \frac{i\gamma}{2}. \tag{3}$$

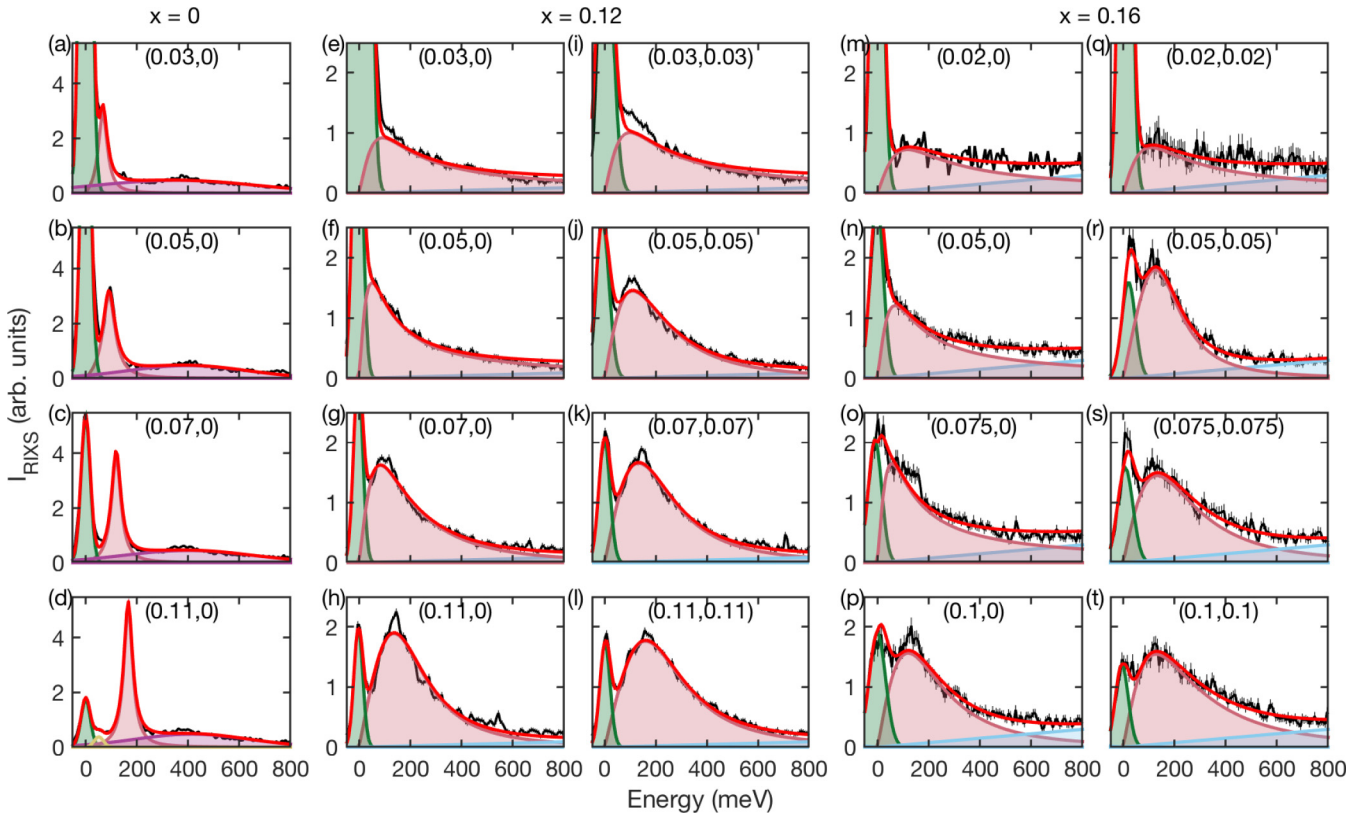

FIG. 3. Examples of fitted RIXS spectra from LCO and LSCO $x = 0.12$ (performed at I21 at DLS) and $x = 0.16$ (performed at ID32 at the ESRF). Showing data in the low **Q** regime from high symmetry directions $(h, 0)$, (h, h). The data have intensity I_{RIXS} indicating that they are normalized to an integration over the range of the dd excitations g. The total fit to the data is indicated in red, the magnetic excitations in pink, elastic peak in green, multimagnons in purple, and background in blue. (e), (f), (i), (j), (m), (n), (o), and (q) are fitted with the ODHO function.

If $\omega_0^2 \geqslant \gamma^2/4$, ω_1 is real and the frequency of the pole. The solutions (response) correspond to damped oscillations in time. If $\omega_0^2 \leqslant \gamma^2/4$, ω_1 is imaginary and the system is overdamped. We may introduce a third frequency ω_{max}, defined as the frequency at the peak in $\chi''(\omega)$. This can be shown to be

$$\omega_{\mathrm{max}} = \frac{1}{6}\sqrt{12\omega_0^2 - 6\gamma^2 + 6\sqrt{\gamma^4 - 4\gamma^2\omega_0^2 + 16\omega_0^4}}. \quad (4)$$

Using the DHO function [Eq. (2)] to analyze all of the data allows a consistent model to be applied to the underdamped and overdamped regimes. This is useful when comparing excitations from undoped and doped compositions. In particular, $\gamma/2 > \omega_0$ is allowed in this model, however, beyond critical damping, $\gamma/2 = \omega_0$, the shape of the response function evolves relatively slowly. Furthermore, the fitted values of γ and ω_0 become correlated. This is the case at small $|\mathbf{Q}|$. In the limit of large damping [40] $\gamma/\omega_0 \to \infty$, $\chi''(\mathbf{Q}, \omega)$ can be approximated by the overdamped harmonic oscillator (ODHO) Lorentzian form,

$$\chi''(\mathbf{Q}, \omega) = \frac{\chi'(\mathbf{Q})\Gamma(\mathbf{Q})\omega}{\omega^2 + \Gamma^2(\mathbf{Q})}. \quad (5)$$

Equation (5) only has two parameters, χ' and the relaxation rate $\Gamma = \omega_0^2/\gamma$. We found it convenient to use Eq. (5) in some of the overdamped region. Thus the gray region in Figs. 7 and 8 indicate the low **Q** regime where Eq. (5) is used to fit the data.

III. RESULTS

A. RIXS spectra of $La_{2-x}Sr_xCuO_4$

Figure 1(c) shows example spectra from each composition at $\mathbf{Q} = (0.25, 0)$. The low-energy magnetic spectrum of the parent ($x = 0$) compound (bottom), is dominated by resolution-limited spin-wave excitations. The magnetic excitations in the doped $x = 0.12$ (middle) and $x = 0.16$ (top) compositions are considerably broader as noted in previous studies [7,9–13]. The dd excitations occur in the energy range 1–3 eV. These are considerably broadened and shifted to lower energy in the doped compositions. The spectra are consistent with published lower resolution data [11].

Figure 2 gives an overall picture of the excitations observed in the present study. Figures 3 and 4 show examples of our RIXS data. Spectra such as those in Figs. 3 and 4 are collected together into intensity maps plotted as a function of **Q** and energy in Fig. 2. The strongest feature in Fig. 2(a) is the magnon which disperses to an energy $\sim 355 \pm 34$ meV along $(h, 0)$ in agreement with previous studies [10,20]. The magnetic excitations are much broader in energy for doped compositions as shown in Figs. 2(c)–2(f). Phonons can be seen in the La_2CuO_4 spectra below 100 meV, for example in Fig. 4(c) and also visible in the map plots in Fig. 2. In

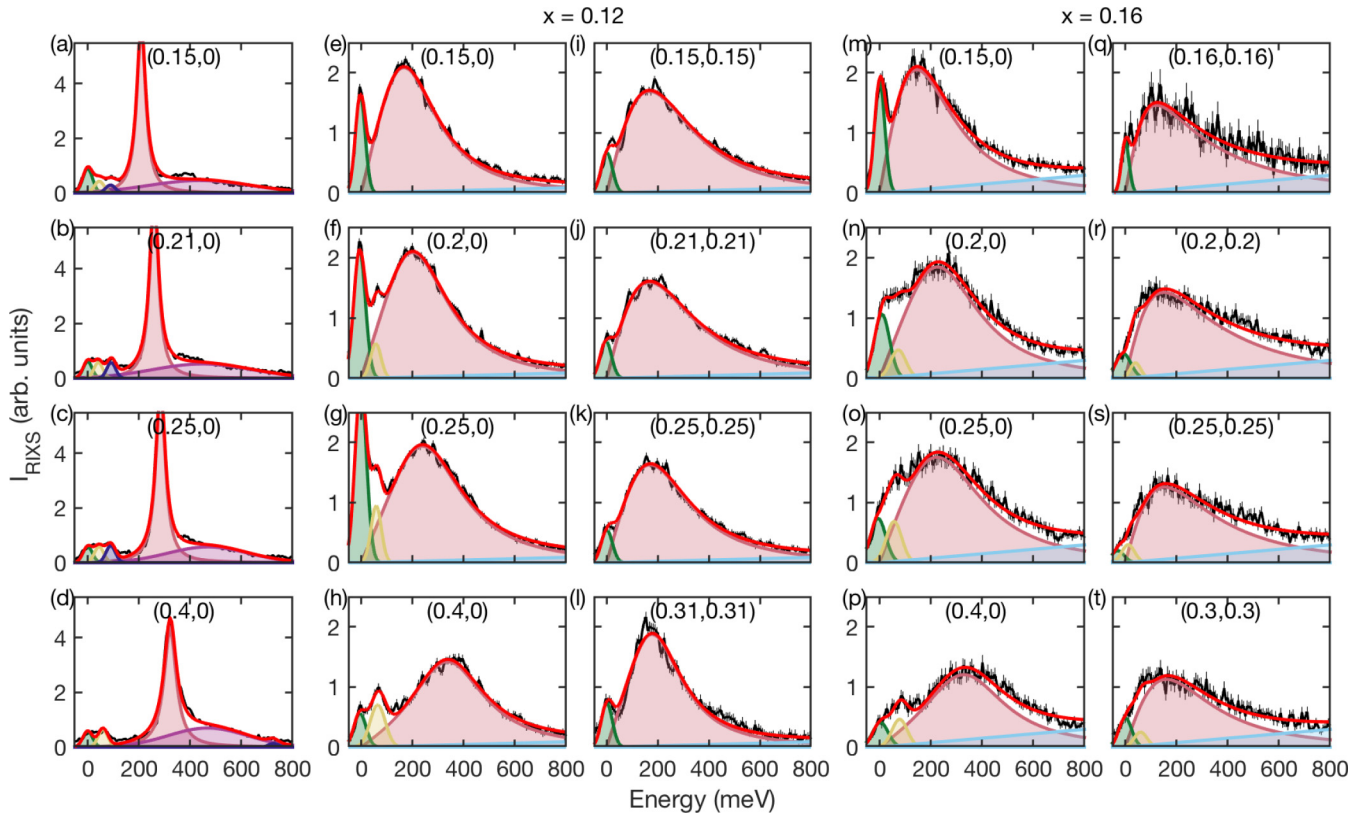

FIG. 4. Examples of fitted RIXS spectra from LCO and LSCO $x = 0.12$ (performed at I21 at DLS) and $x = 0.16$ (performed at ID32 at the ESRF). Showing data in the high **Q** regime from high symmetry directions $(h, 0)$, (h, h). The data have intensity I_{RIXS} indicating that they are normalized to an integration over the range of the dd excitations g. The total fit to the data is indicated in red, the DHO magnetic excitations in pink, elastic peak in green, phonon excitations in yellow and dark blue, multimagnons in purple, and background in light blue.

Fig. 2(c), for $x = 0.12$ and 0.16, a particularly strong phonon branch can be seen below 100 meV along $(h, 0)$ near $h = 0.3$. This indicates coupling to charge excitations. In the $x = 0.12$ composition, CDW order is seen near $h = 0.23$. Similar behavior [41] is seen in $Bi_2Sr_2CaCu_2O_{8+\delta}$.

In addition to the high-symmetry direction measurements shown in Figs. 2 and 3, a full quadrant of the Brillouin zone was examined by mapping (h, k) in the $x = 0.16$ and 0.12 compounds. Approximately 90 spectra were collected at the ID32 beamline, distributed throughout the zone with spacing 0.05 (r.l.u.). The RIXS intensity is plotted as a function of (h, k) for several energy slices and for $x = 0.12$ in Fig. 5 where areas of high-intensity correspond to the spin-excitation intensity. These measurements were performed with lower resolution ($\Delta E \simeq 50$ meV). The plots are smoothed by averaging neighboring points within $|\Delta\mathbf{Q}| = 0.05$ r.l.u. At low energies, the maximum in the RIXS intensity appears at low **Q** and is approximately symmetrically distributed around Γ. As the energy increases, peaks develop along $(h, 0)$ and $(0, k)$ and move to larger h and k. It is interesting to note that quite similar behavior is observed [20] in La_2CuO_4, where (h, k) maps measured with INS show a peak in the intensity at $(\frac{1}{2}, 0)$ for energies above about 320 meV. The maps show that for doped LSCO the magnetic spectral weight persists

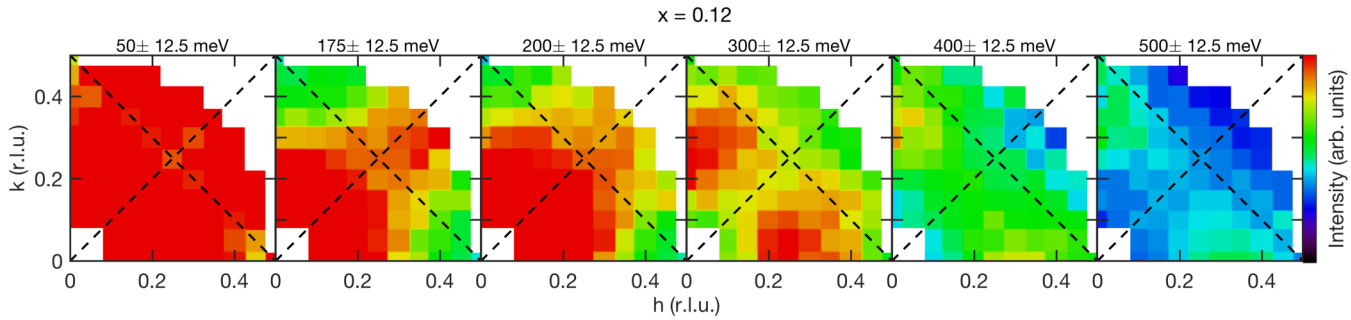

FIG. 5. Constant energy maps of RIXS intensity as a function of **Q** vector (h, k) in LSCO $x = 0.12$. The data have intensity I_{RIXS} indicating that they are normalized to an integration over the range of the dd excitations g. Measurements were performed at ID32 at the ESRF with $\Delta E \simeq 50$ meV. Black dashed lines indicate the zone boundary and high symmetry directions.

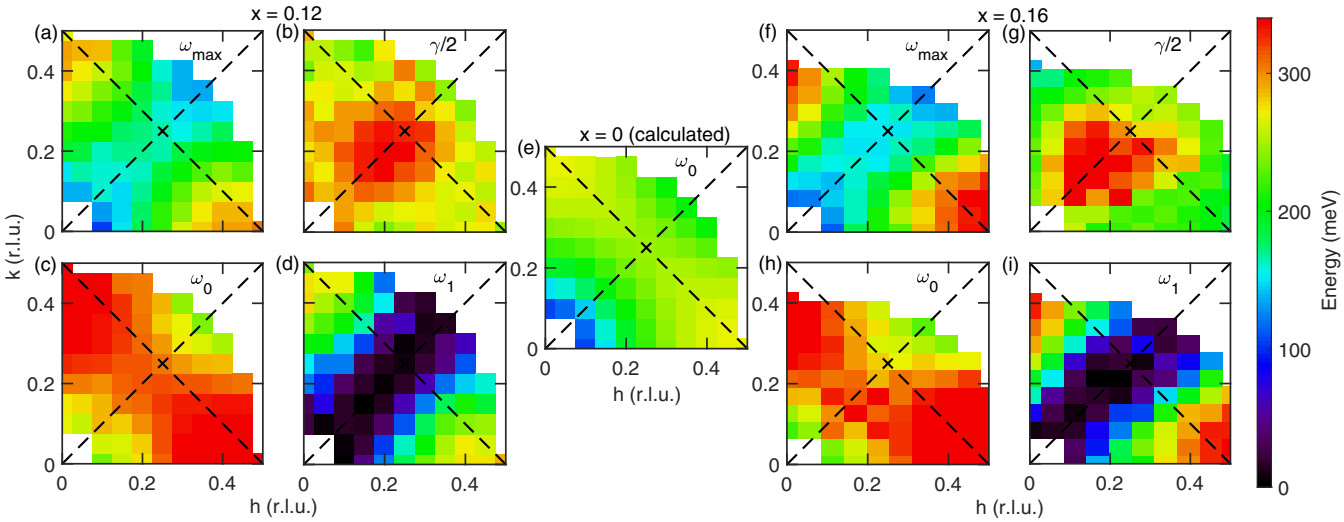

FIG. 6. Map plots showing the parameters of a damped harmonic oscillator fit as a function of wave-vector **Q** in $x = 0.12$ and $x = 0.16$ LSCO. Measurements were performed at ID32 at the ESRF with $\Delta E \simeq 50$ meV. Showing the maximum of the magnon peak ω_{max} in (a) and (f), the damping factor $\gamma/2$ in (b) and (g), and the magnon poles ω_0 in (c) and (h) and ω_1 in (d) and (i). The equivalent magnon pole ω_0 calculated for $x = 0$ from linear spin-wave theory with parameters from INS is shown in (e). Black dashed lines indicate the zone boundary and high symmetry directions.

to higher energies near $(\frac{1}{2}, 0)$ than in other parts of the Brillouin zone. This observation is consistent with previous work [7,11–13,26].

B. DHO fitting

Figures 3 and 4 show fits of the damped harmonic oscillator (DHO) model (Sec. II D) together with phonon peaks and background to the data. The 35 meV resolution of the instrument allows the phonons and elastic peaks to be separated from the DHO response. For example, in La_2CuO_4 the frequencies are approximately wave vector independent with energies ∼45 and 90 meV which are attributed to CuO bond-bending and bond-stretching modes, respectively [42–44]. As can be seen from the figures, the DHO model generally describes the magnetic excitations well. The measured spectra are shown in black with the total fitted function indicated in red with constituent functions below. The parameters ω_0 and $\gamma/2$ extracted from DHO fits are plotted for $\mathbf{Q} = (h, 0)$ and (h, h) in Fig. 7 for each compound. Equation (5) is used to fit the small **Q** (gray) regime and the resulting relaxation rate Γ is shown. Hole doping the parent compound increases $\gamma/2$. In the doped compounds, it can be comparable to ω_0. The damping is anisotropic in wave vector [11–13,26], that is $\gamma/2$ is larger along (h, h) than along $(h, 0)$. Our data also reveals that the anisotropy of the damping does not reflect the antiferromagnetic Brillouin zone as $\gamma/2$ peaks at approximately (0.2, 0.2) [rather than $(\frac{1}{4}, \frac{1}{4})$] along (h, h). This effect can be seen both for $x = 0.12$ and $x = 0.16$ [Figs. 7(d) and 7(f)].

We also fit the lower resolution ($\Delta E \simeq 50$ meV) spectra from the grid in (h, k). The results of fitting this data to the DHO model are summarized in Fig. 6. The damping $\gamma/2$ is again seen to be largest in the region near (0.2,0.2) for both doped compositions. The overdamped region where $\omega_0^2 < \gamma^2/4$ and ω_1 is imaginary, is indicated in Figs. 6(d) and 6(i) as $\omega_1 = 0$.

It should be noted that normalizing the data to an integration over the range of the dd excitations does not account for the energy dependence of the self-absorption. The line shape of the excitation is therefore altered by the strong absorption of the scattered photons at low energy. We calculated that the damping parameters γ is reduced by approximately 24% as a result of accounting for the energy-dependent self-absorption [45]. This reduction decreases slightly with **Q**, and therefore the key result, that $\gamma/2$ is peaked in **Q** away from $(\frac{1}{4}, \frac{1}{4})$, is unaffected.

C. Estimate of the absolute wave vector dependent susceptibility

Fitting our RIXS data to the DHO response function in Eq. (2) allows the wave vector dependent susceptibility $\chi'(\mathbf{Q})$ to be estimated, where

$$\chi'(\mathbf{Q}) = \chi'(\mathbf{Q}, \omega = 0) = \frac{1}{\pi} \int_{-\infty}^{\infty} \frac{\chi''(\mathbf{Q}, \omega)}{\omega} \, d\omega. \quad (6)$$

In this section we estimate $\chi'(\mathbf{Q})$ in the superconductors we have investigated by using the parent antiferromagnet La_2CuO_4 as a reference. This estimation assumes that the DHO response contains only magnetic contributions which is somewhat justified by recent polarization analysis [33,34]. The data of Peng *et al.* suggest that approximately 82% of spectral weight is magnetic in the region of the magnetic excitations, 150–600 meV. In our analysis, the 18% charge contribution is partially accounted for in the background and multimagnon fits but any remaining charge contribution may lead to an overestimation of $\chi'(\mathbf{Q})$.

The analysis discussed so far has relied on normalization to g, an integration over the region of the dd excitations, to take account of angle-dependent effects on the RIXS intensity. This does not affect the determination of excitation energies or damping coefficients. However, this procedure does not account for the difference in absorption between photons

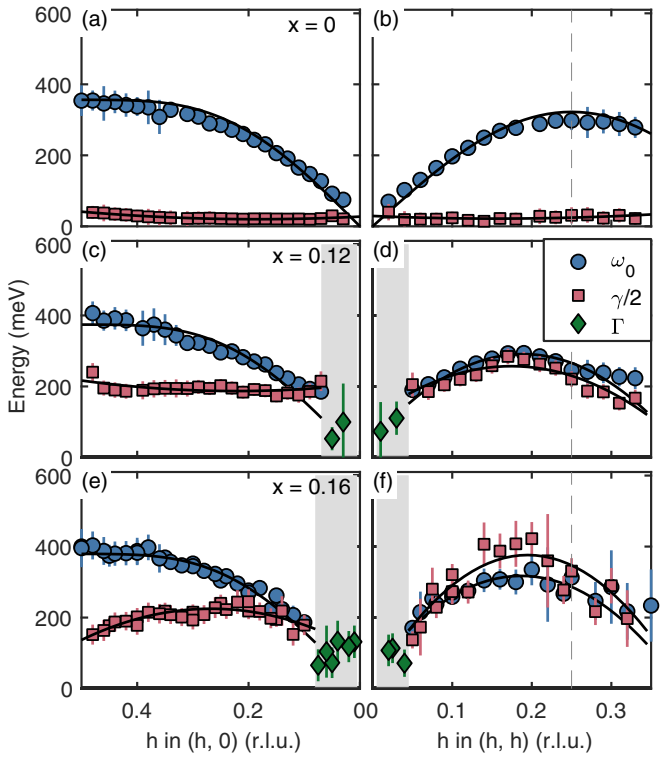

FIG. 7. Summary of fit parameters to a DHO response model as a function of wave-vector **Q** along high symmetry directions $(h, 0)$ and (h, h). ω_0 is indicated with blue circles and the damping coefficient $\gamma/2$ is shown as red squares. In the low **Q** regime the ODHO relaxation rate is given by Γ which is shown as green diamonds. Errors are from fitting considering the standard error in the raw data. Solid lines are a cubic polynomial fit to the data. Data in (a), (b), and (c) all contain data measured at I21 and (c) contains additional data measured at ID32. The dashed gray line marks the AF Brillouin zone boundary.

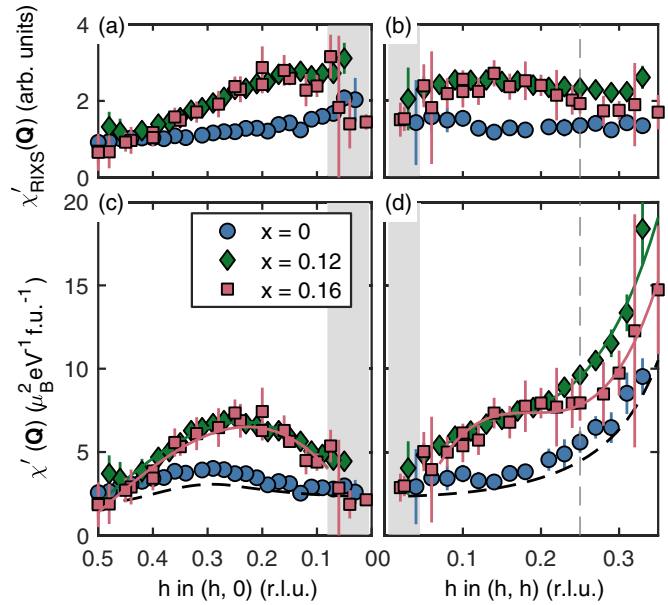

FIG. 8. Wave vector dependent susceptibilities $\chi'(\mathbf{Q})$ in $La_{2-x}Sr_xCuO_4$ determined from RIXS spectra. Fits of a damped harmonic oscillator function to I_{RIXS} yield estimates of $\chi'_{\mathrm{RIXS}}(\mathbf{Q})$ shown in (a) and (b) which include self-absorption and other orientation-dependent effects. (c) and (d) Estimates of the absolute $\chi'(\mathbf{Q})$. These estimates are obtained by normalizing the data from doped compositions by the antiferromagnetic parent compound as described in the text. Cubic polynomial fits to the data are shown as solid lines and the dashed line shows the SWT model. The dashed gray line indicates the Brillouin zone boundary. Data on all compounds were collected at I21 and additional data on the $x = 0.16$ compound were measured at ID32.

scattered from the magnetic excitations, which are close to the resonance, and the dd excitations which are significantly away from the Cu absorption peak (with a width of about 0.4 eV) and are therefore less likely to be absorbed. In order to correct for these effects, we use the measured spin wave RIXS intensity of the parent compound as a reference. INS measurements show that the magnetic excitations of La_2CuO_4 are fairly well described by linear spin wave theory (SWT) with some corrections [20] near $(\frac{1}{2}, 0)$. Thus the underlying $S(\mathbf{Q}, \omega)$ is known in this case.

Ament *et al.* [5] point out that under certain theoretical approximations, the absolute RIXS cross section can be split into a prefactor $f(\boldsymbol{\epsilon}, \boldsymbol{\epsilon}', \mathbf{k}, \mathbf{k}')$ multiplied by a dynamic structure factor $S(\mathbf{Q}, \omega)$, where the polarizations of the initial and final photons are $\boldsymbol{\epsilon}$ and $\boldsymbol{\epsilon}'$. We note that the exact circumstances when the RIXS response is proportional to $S(\mathbf{Q}, \omega)$ is still an active subject of investigation [5,38], however, we will use this approximation in our analysis. Here we propose a simple estimate to remove the effects of $f(\boldsymbol{\epsilon}, \boldsymbol{\epsilon}', \mathbf{k}, \mathbf{k}')$ from $S(\mathbf{Q}, \omega)$ for doped LSCO. We assume $f(\boldsymbol{\epsilon}, \boldsymbol{\epsilon}', \mathbf{k}, \mathbf{k}')$ is the same for doped and undoped compounds. For each $(\mathbf{k}, \mathbf{k}')$ we first normalize (divide) the raw RIXS spectra by g to yield I_{RIXS} (see Sec. II D) and find χ'_{RIXS} by fitting to the DHO model. We then multiply χ'_{RIXS} for LSCO by the spin-wave response of LCO determined from INS [20] divided by the measured RIXS response of LCO, to estimate the dynamic susceptibility of the doped superconductor in absolute units:

$$\langle \chi'^{\mathrm{LSCO}}(\mathbf{Q}) \rangle = \chi'^{\mathrm{LSCO}}_{\mathrm{RIXS}}(\mathbf{Q}) \times \frac{\phi^{\mathrm{LCO}}_{\mathrm{SWT}}(\mathbf{Q})}{\phi^{\mathrm{LCO}}_{\mathrm{RIXS}}(\mathbf{Q})}. \tag{7}$$

$\phi^{\mathrm{LCO}}_{\mathrm{SWT}}$ is the energy integrated spin-wave pole weight, determined from a fit of linear SWT to INS data and $\phi^{\mathrm{LCO}}_{\mathrm{RIXS}}$ is the integrated pole weight of fitted RIXS data, details of this are given in the Appendix. In practice, we fit the LCO spectra and then use Eqs. (A5) and (A7) to evaluate $\phi^{\mathrm{LCO}}_{\mathrm{SWT}}$ and $\phi^{\mathrm{LCO}}_{\mathrm{RIXS}}$. Equation (7) assumes that the factors f and g are the same in doped and undoped compositions and therefore cancel in the normalization procedure. We have verified that this is approximately the case in our samples.

Figures 7, 8(a), and 8(b) show the parameters $\gamma(\mathbf{Q})$, $\omega_0(\mathbf{Q})$, and $\chi'(\mathbf{Q})$ extracted from fits of Eq. (2) as a function of **Q** along $(h, 0)$ and (h, h) for the three compounds. For LCO, $\chi''(\mathbf{Q}, \omega)$ is a sum of the single and multimagnon contributions. For LSCO, a single response function is used. The resulting $\chi'_{\mathrm{RIXS}}(\mathbf{Q})$ due to the magnon pole is shown in Figs. 8(a) and 8(b) with a cubic polynomial fit indicated with a solid blue line. The susceptibilities $\chi'_{\mathrm{RIXS}}(\mathbf{Q})$ in Figs. 8(a) and 8(b) contain the effects of the f factor and self-absorption

TABLE I. Doping dependence of the $\chi'(\mathbf{Q})$ in LSCO as measured with RIXS.

Q	(1/4, 0)	(1/4, 1/4)
x	$\chi'(\mathbf{Q})(\mu_B^2\,\mathrm{eV}^{-1}\,\mathrm{f.u.}^{-1})$	
0	3.7 ± 0.3	5.6 ± 0.6
0.12	7.1 ± 0.3	9.6 ± 1
0.16	7.3 ± 0.8	8.0 ± 1

mentioned above. In Figs. 8(c) and 8(d) we correct for these effects and estimate the absolute $\chi'(\mathbf{Q})$ using Eqs. (7), (A5), and (A7) together with the cubic polynomial fit of $\chi'_{\mathrm{RIXS}}(\mathbf{Q})$ to La_2CuO_4 in Figs. 8(a) and 8(b).

By definition, the corrected susceptibility for the parent compound La_2CuO_4 becomes that of the SWT model described in the Appendix plus additional spectral weight due to the multimagnon excitations observed with RIXS. For all three compositions investigated, $\chi'(\mathbf{Q})$ increases as we move along (h, h) towards $(\frac{1}{2}, \frac{1}{2})$, where INS finds the strongest spin fluctuations. The magnitude of $\chi'(\mathbf{Q})$ is generally larger for the doped compositions $x = 0.12, 0.16$ than in the parent (see Table I and Fig. 8), this effect is also present when the data are normalized via the dd excitations so it does not seem to be an artifact arising from the spin wave normalization. The increase arises when spectral weight in $\chi''(\mathbf{Q}, \omega)$ is moved to lower energy and gives a larger contribution to $\chi'(\mathbf{Q})$ because of the $1/\omega$ factor in Eq. (6). For example, if, for a particular $\mathbf{Q}$, a spin wave keeps the same integrated intensity in $\chi''(\mathbf{Q}, \omega)$ and is broadened in ω, then $\chi'(\mathbf{Q})$ can increase. Inspection of Fig. 4 shows that this indeed happens. The modeled excitations are shown in Fig. 9 where $\chi''(\mathbf{Q}, \omega)$ is calculated from Eq. (2) with the fitted parameters $[\omega_0(\mathbf{Q}), \gamma(\mathbf{Q}), \chi'(\mathbf{Q})]$ shown in Figs. 7, 8(c), and 8(d).

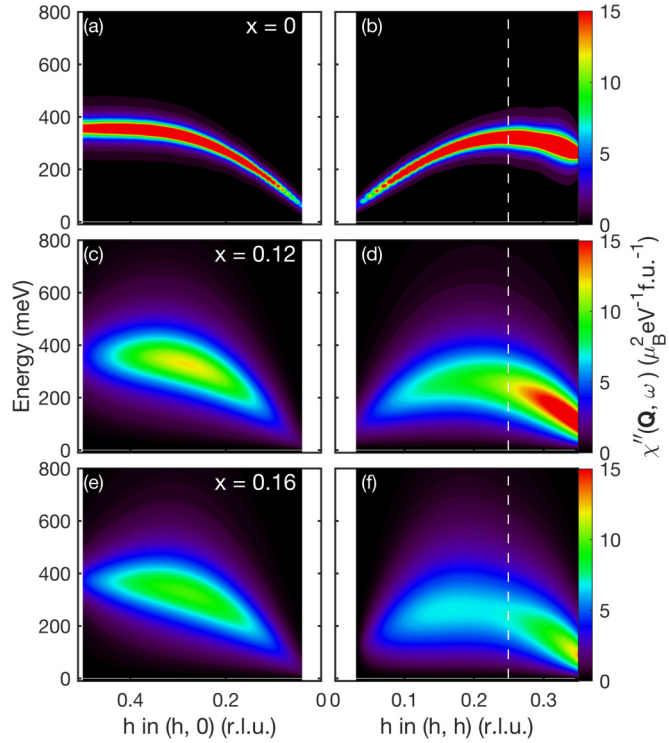

FIG. 9. (a)–(f) Intensity plots of $\chi''(\mathbf{Q}, \omega)$ showing the modeled excitations using the fitted parameters $[\omega_0(\mathbf{Q}), \gamma(\mathbf{Q}), \chi'(\mathbf{Q})]$ from Figs. 7 and 8 with Eq. (2).

IV. DISCUSSION

A. Theoretical models

Our investigation of the magnetic excitations in cuprates is motivated by spin-fluctuation mediated theories of high temperature superconductivity [2] and to gain a fundamental understanding of metallic transition metal oxides. The Hubbard model (in its one- or three-band variants) is generally considered to be a good starting point. Calculations based on the Hubbard model [2] show that the wave vector dependent pairing interaction V_{eff} is approximately [2,46]

$$V_{\mathrm{eff}} \simeq \tfrac{3}{2}U^2\chi'(\mathbf{p}' - \mathbf{p}), \tag{8}$$

where $\mathbf{p}'$ and $\mathbf{p}$ are the wave vectors of the two electrons making up a Cooper pair and U is the Hubbard on-site interaction. RIXS measurements of the magnetic excitations over a wide energy range allow us the opportunity to determine $\chi'(\mathbf{q})$. This can be used as an input to theory or a test of models of the excitations. Numerical studies of the two-dimensional Hubbard model, applied to cuprates, qualitatively reproduce [47] the slowly evolving high-energy magnetic excitations which are observed by INS and RIXS experiments, but calculations are restricted to relatively small lattices. Other approaches based on renormalized itinerant quasiparticles [13,48–50] with various types of approximation provide a basis for a phenomenological understanding of the physical properties and allow finer structure in wave vector and energy to be predicted. In general, we expect the magnetic excitations and $\chi''(\mathbf{Q}, \omega)$ to be different around (0,0) and $(\frac{1}{2}, \frac{1}{2})$ and the dispersion of the excitations not to be symmetric around $(\frac{1}{4}, \frac{1}{4})$.

B. Wave vector dependence of the response

The high-energy magnetic excitations in the parent compound La_2CuO_4 are anisotropic in two ways. First, the single magnon energy varies between points on the antiferromagnetic Brillouin zone boundary with $(\frac{1}{2}, 0)$ having a higher energy than $(\frac{1}{4}, \frac{1}{4})$. Second, the single magnon excitation is strongly and anomalously damped at the $(\frac{1}{2}, 0)$ position. This variation in the magnon energy can be understood in terms of an expansion of the single band Hubbard model [19,51] which gives rise to second nearest neighbor and cyclic exchange interactions. While the anisotropy of the damping in La_2CuO_4 may be understood in terms of the unbinding of magnons into spinons [20,52]. This is a generic property [20,52] of $S = 1/2$ square lattice antiferromagnets.

Our data show how the anisotropies of the parent compound persist into the doped compositions and are qualitatively consistent with previous studies [11,13,26]. However, the higher energy resolution of the present study ($\Delta E \approx 35$ meV as compared to $\Delta E \gtrsim 100$ meV in previous work [11,13,26]) allows us to separate the magnetic excitations from lower energy features. In Fig. 7 we see that

the frequency of the undamped mode $\omega_0(\mathbf{Q})$ extracted from the DHO model shows similar dispersions along $(h, 0)$ and (h, h) in the doped $x = 0.12$ and $x = 0.16$ compositions as in the parent $x = 0$. At $\mathbf{Q} = (\frac{1}{2}, 0)$, $\hbar\omega_0$ increases with doping from 356 ± 45 ($x = 0$) to 396 ± 54 meV ($x = 0.16$), while at $\mathbf{Q} = (\frac{1}{4}, \frac{1}{4})$ it increases from 298 ± 27 to 313 ± 30 meV.

A new result from this work is the extent of the variation of $\gamma(\mathbf{Q})$ and $\omega_0(\mathbf{Q})$ across the Brillouin zone in doped LSCO. Significantly, the damping is seen to increase in the underdoped compound $x = 0.12$ and again in the optimally doped material $x = 0.16$. From the damping maps shown in Figs. 6(b) and 6(g) it can be seen that the enhanced damping is most prominent close to the (h, h) direction. It is notable that the maxima in $\gamma(\mathbf{Q})$ and $\omega_0(\mathbf{Q})$ along (h, h) are actually near (0.2,0.2) rather than at $(\frac{1}{4}, \frac{1}{4})$. Our (h, k) maps of the fitted parameters in Fig. 6 show that $\gamma(\mathbf{Q})$ actually shows a local maximum around this point. These features appear to be qualitatively present in theoretical calculations based on itinerant quasiparticle such as those in Refs. [13,50] and presumably arise from (nesting) features in the underlying quasiparticle band structure. The general damping anisotropy between $(h, 0)$ and (h, h) for the doped compositions has also been described by theories based on determinantal quantum Monte Carlo (DQMC) [47].

The normalization procedure described in Sec. III C allows us to obtain the estimates of $\chi'(\mathbf{Q})$ in Fig. 8. Values of χ' at representative wave vectors are shown in Table I. A striking feature of the analysis is that it shows that there is a large anisotropy in $\chi'(\mathbf{Q})$ at the antiferromagnetic Brillouin zone boundary. In particular, $\chi'(\mathbf{Q})$ is about 4 times larger at $(\frac{1}{4}, \frac{1}{4})$ than at $(\frac{1}{2}, 0)$. This arises because of the smaller $\omega_0(\mathbf{Q})$ at $(\frac{1}{4}, \frac{1}{4})$ (see Figs. 4 and 7) which shifts spectral weight to lower energy.

A maximum on $\chi'(\mathbf{Q})$ along $(h, 0)$ is seen for all compositions. This may derive from the combination of two effects present in the parent antiferromagnetic state. First, linear spin-wave theory of a square lattice $S = 1/2$ antiferromagnet (see the Appendix) predicts that $\chi'(\mathbf{Q})$ increases from (0,0) to $(\frac{1}{2}, 0)$. Second, square lattice $S = 1/2$ antiferromagnets such as La_2CuO_4 [20] and CFDT [52] show anomalous broadening and weakening of their magnetic excitations near $(\frac{1}{2}, 0)$ and thus a dip in $\chi'(\mathbf{Q})$ at this position. This is not predicted in the pure SWT model and has been understood in terms of the unbinding of magnons into spinon pairs [52]. Our results suggest that these effects persist for doped compositions.

Also of interest is the fact that $\chi'(\mathbf{Q})$ increases monotonically along (h, h) from Γ to M. The increase is consistent with the fact that the magnetic response is strongest in the antiferromagnetic Brillouin zone centered on M. This is expected because of the residual antiferromagnetic exchange interactions and is qualitatively consistent with INS measurements [16,21,23–25]. Thus, to our knowledge, Figs. 8(c) and 8(d) are the first attempts to determine $\chi'(\mathbf{Q})$ in absolute units based on integrals of the magnetic response over a wide energy range. It should be noted that theoretical calculations based on the Hubbard model [46,47] show that spin fluctuation in the M zone contribute most to pairing in spin-fluctuation mediated theories of HTC. Figure 9 shows the total modeled excitation for all compositions. The wave vector dependence of the susceptibility and damping is clearly shown.

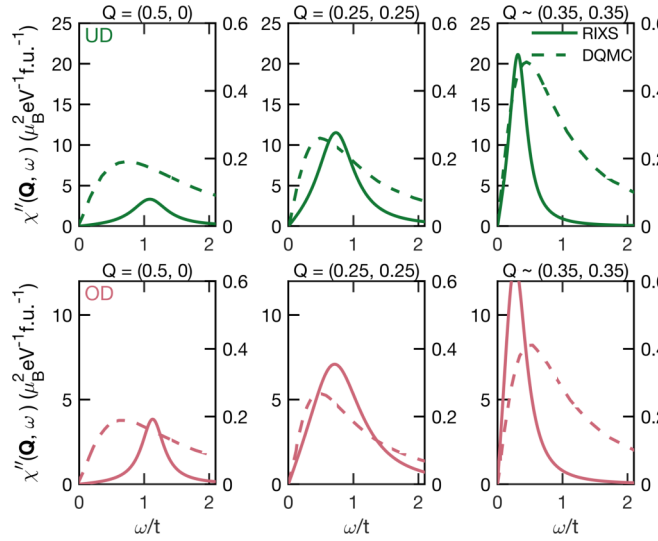

FIG. 10. Comparison of $\chi''(\mathbf{Q})$ modeled from the RIXS parameters and calculations in DQMC by Huang *et al.* [47]. Showing our modeled spectra from the $x = 0.12$ compound (solid green line) compared to calculations at $x = 0.1$ (dashed green line) and spectra from the $x = 0.16$ compound (solid pink line) compared to calculations at $x = 0.15$ (dashed pink line). The plots are scaled differently, the RIXS scale is shown on the left axis and the DQMC scale is shown on the right.

In Fig. 10 we compare slices with calculations from the DQMC calculations of Huang *et al.* [47]. The DQMC calculations reproduce qualitatively some of the features of our data such as the increase in the strength of $\chi''(\mathbf{Q}, \omega)$ moving towards $(\frac{1}{2}, \frac{1}{2})$. However, the RIXS spectra are generally much sharper and show a stronger wave vector dependence.

C. Comparison to INS

RIXS and INS provide complementary views of the collective spin excitations in the cuprates [24]. However, INS measurements of the high-energy magnetic excitations are difficult because the background increases when high incident energies are used. Nevertheless, some data does exist for $La_{2-x}Sr_xCuO_4$. An early study [16] on $La_{1.86}Sr_{0.14}CuO_4$ revealed magnetic excitations up to 260 meV. In particular, excitations were observed at $\mathbf{Q} = (\frac{3}{2}, 0)$ which is equivalent to the $\mathbf{Q} = (\frac{1}{2}, 0)$ position investigated here with RIXS. Our RIXS normalization procedure (Sec. III C) allows us to estimate $\chi'(\mathbf{Q}) = 1.8 \pm 0.6\ \mu_B^2\,\mathrm{eV}^{-1}\,\mathrm{f.u.}^{-1}$ in LSCO $x = 0.16$ at $(\frac{1}{2}, 0)$ based on an integration of the spectrum up to about 800 meV. Integrating the INS data in Ref. [16] up to 260 meV we obtain $\chi'(\mathbf{Q}) \approx 0.5\ \mu_B^2\,\mathrm{eV}^{-1}\,\mathrm{f.u.}^{-1}$. Thus, if it were possible to perform neutron scattering experiments over a wider energy range the integration of INS data may produce a comparable value for $\chi'(\mathbf{Q})$ at $\mathbf{Q} = (\frac{1}{2}, 0)$. The approximate agreement is satisfying, however further work is required to develop the comparison of the two probes of collective magnetic excitations.

The INS study in Ref. [16] [Fig. 4(d)] also estimated $\chi'(\mathbf{Q})$ along the line (h, h) for $La_{1.86}Sr_{0.14}CuO_4$. Unfortunately,

the energy integration was only carried out over the range $0 \leqslant \hbar\omega \leqslant 150$ meV. However, the increase in $\chi'(\mathbf{Q})$ in the doped compound in the range $0.25 \leqslant h \leqslant 0.34$ [Fig. 8(d), present paper] is also seen with INS. The absolute values of $\chi'(\mathbf{Q})$ measured with neutrons are of the same order of magnitude but less than those reported in the present RIXS study presumably because the INS study integrates only up to 150 meV.

V. SUMMARY AND CONCLUSIONS

We have made high-resolution RIXS measurements of the collective magnetic excitations for three compositions of the superconducting cuprate system $La_{2-x}Sr_xCuO_4$. Specifically, we have mapped out the excitations throughout the 2D (h, k) Brillouin zone to the extent that is possible at the Cu-L edge. In addition, we have attempted to determine the wave vector dependent susceptibility of the doped compositions $La_{2-x}Sr_xCuO_4$ $(x = 0.12, 0.16)$ by normalizing data to the parent compound. This procedure allows comparison with INS measurements. We find that the evolution of the intensity of high-energy ($\hbar\omega \gtrsim 200$ meV) excitations measured by RIXS and INS is consistent.

The high-energy spin fluctuations in $La_{2-x}Sr_xCuO_4$ are fairly well described by a damped harmonic oscillator model. The DHO damping parameter increases with doping and is largest along the (h, h) line although it is not peaked at the high symmetry point $(\frac{1}{4}, \frac{1}{4})$. While the pole frequency is peaked at $(\frac{1}{2}, 0)$ for doped and undoped compositions, for the doped compositions, the wave vector dependent susceptibility $\chi'(\mathbf{Q})$ is much larger at $(\frac{1}{4}, \frac{1}{4})$ than at $(\frac{1}{2}, 0)$. Both of these positions are on the antiferromagnetic zone boundary of the parent compound. The wave vector dependent susceptibility increases rapidly along the (h, h) line towards the antiferromagnetic wave vector of the parent compound $(\frac{1}{2}, \frac{1}{2})$. Thus the strongest magnetic excitations and those predicted to favor superconductive pairing occur towards the $(\frac{1}{2}, \frac{1}{2})$ position. Our quantitative determination of the wave vector dependent susceptibility will be useful in testing magnetic mediated theories of high-temperature superconductivity [1,2].

ACKNOWLEDGMENTS

The authors acknowledge funding and support from the Engineering and Physical Sciences Research Council (EPSRC) Centre for Doctoral Training in Condensed Matter Physics (CDT-CMP), Grant No. EP/L015544/1 as well as Grant No. EP/R011141/1. We acknowledge Diamond Light Source for time on Beamline I21 under proposals SP18469 and SP18512 and the European Synchrotron Radiation Facility for time on Beamline ID32 under proposal HC/2696. We would like to thank G. B. G. Stenning and D. W. Nye for help on the Laue instrument in the Materials Characterisation Laboratory at the ISIS Neutron and Muon Source.

APPENDIX: LINEAR SPIN-WAVE THEORY CALCULATIONS

The magnetic excitations can be modeled in LCO with classical linear spin-wave theory. We consider the case of a $S = 1/2$ square lattice antiferromagnet with nearest- and next-nearest exchange interactions. The susceptibility transverse to the ordered moment $\chi''_\perp(\mathbf{Q}, \omega)$ due to one-magnon creation is given by

$$\chi''_\perp(\mathbf{Q}, \omega) = Z_d(\mathbf{Q})\frac{\pi}{2}g^2\mu_B^2 S\left(\frac{A_\mathbf{Q} - B_\mathbf{Q}}{A_\mathbf{Q} + B_\mathbf{Q}}\right)^{1/2}\delta[\omega \pm \omega_0(\mathbf{Q})]$$
$$= \frac{\pi}{2}\chi'_\perp(\mathbf{Q})\,\omega_0(\mathbf{Q})\delta[\omega \pm \omega_0(\mathbf{Q})], \tag{A1}$$

where

$$\hbar\omega_0(\mathbf{Q}) = 2Z_c\sqrt{A_\mathbf{Q}^2 - B_\mathbf{Q}^2} \tag{A2}$$

and

$$\chi'_\perp(\mathbf{Q}) = Z_d(\mathbf{Q})\frac{g^2\mu_B^2 S}{A_\mathbf{Q} + B_\mathbf{Q}}. \tag{A3}$$

The amplitude factors $A_\mathbf{Q}$ and $B_\mathbf{Q}$ are given [19] by $A_\mathbf{Q} = J - J_c/2 - (J' - J_c/4)(1 - v_h v_k) - J''[1 - (v_{2h} + v_{2k})/2]$, $B_\mathbf{Q} = (J - J_c/2)(v_h + v_k)/2$, where $v_x = \cos(2\pi x)$ and $x \mapsto h$ or k. Z_d and Z_c are renormalization constants which take account of quantum fluctuations in the AF ground state.

Headings *et al.* [20] have made INS measurements of the spin waves in La_2CuO_4 and fitted the model described by Eqs. (A1)–(A3). They find $J = 143$, $J' = J'' = 2.9$, and $J_c = 58$ meV, assuming $Z_c = 1.18$. The wave vector dependence of $Z_d(\mathbf{Q})$ is also determined from the INS data,

$$Z_d(\mathbf{Q}) = \begin{cases} Z_{d0}\sin(h\pi), & \text{if } h < \frac{1}{4}, \\ Z_{d0}\sin\left(\frac{\pi}{4}\right), & \text{if } h \geqslant \frac{1}{4}, \end{cases} \tag{A4}$$

where $Z_{d0} = 0.4$. In order to compare the INS and RIXS measurements, we assume that RIXS is equally sensitive to the three components of the susceptibility and compute the average susceptibility $\chi = \frac{1}{3}(\chi_{xx} + \chi_{yy} + \chi_{zz}) = \frac{2}{3}\chi_\perp$. The energy integrated intensity of the spin wave pole $\phi^{\mathrm{LCO}}_{\mathrm{SWT}}(\mathbf{Q})$ is then

$$\phi^{\mathrm{LCO}}_{\mathrm{SWT}}(\mathbf{Q}) = \int_0^\infty \chi''(\mathbf{Q}, \omega)\,d\omega = \frac{\pi}{3}\chi'_\perp(\mathbf{Q})\,\omega_0(\mathbf{Q}). \tag{A5}$$

We derive a comparable measure of the energy integrated spin-wave pole measured with RIXS by rewriting Eq. (2) for LCO (in the limit $\omega_0 \geqslant \gamma/2$) as

$$\chi''(\mathbf{Q}, \omega) = \frac{\chi'(\mathbf{Q})}{2\omega_1(\mathbf{Q})}\left[\frac{\gamma^2(\mathbf{Q})}{4} + \omega_1^2(\mathbf{Q})\right]$$
$$\times\left\{\frac{\gamma(\mathbf{Q})/2}{\gamma^2(\mathbf{Q})/4 + [\omega - \omega_1(\mathbf{Q})]^2}\right.$$
$$\left. - \frac{\gamma(\mathbf{Q})/2}{\gamma^2(\mathbf{Q})/4 + [\omega + \omega_1(\mathbf{Q})]^2}\right\}. \tag{A6}$$

Integrating over the positive energy pole, we obtain the measured pole intensity from the fitted parameters $\omega(\mathrm{Q})$, $\gamma(\mathrm{Q})$, and $\chi'(\mathrm{Q})$:

$$\phi^{\mathrm{LCO}}_{\mathrm{RIXS}}(\mathbf{Q}) = \frac{\pi\chi'(\mathbf{Q})\omega_0^2(\mathbf{Q})}{\sqrt{4\omega_0^2(\mathbf{Q}) - \gamma^2(\mathbf{Q})}}. \tag{A7}$$

[1] A. V. Chubukov, D. Pines, and J. Schmalian, A spin fluctuation model for d-wave superconductivity, in *The Physics of Superconductors: Vol. I. Conventional and High-Tc Superconductors*, edited by K. H. Bennemann and J. B. Ketterson (Springer, Berlin, 2003), pp. 495–590.

[2] D. J. Scalapino, Rev. Mod. Phys. **84**, 1383 (2012).

[3] M. Eschrig, Adv. Phys. **55**, 47 (2006).

[4] B. Keimer, S. A. Kivelson, M. R. Norman, S. Uchida, and J. Zaanen, Nature (London) **518**, 179 (2015).

[5] L. J. P. Ament, M. van Veenendaal, T. P. Devereaux, J. P. Hill, and J. van den Brink, Rev. Mod. Phys. **83**, 705 (2011).

[6] L. Braicovich, L. J. P. Ament, V. Bisogni, F. Forte, C. Aruta, G. Balestrino, N. B. Brookes, G. M. De Luca, P. G. Medaglia, F. Miletto Granozio, M. Radovic, M. Salluzzo, J. van den Brink, and G. Ghiringhelli, Phys. Rev. Lett. **102**, 167401 (2009).

[7] L. Braicovich, J. van den Brink, V. Bisogni, M. M. Sala, L. J. P. Ament, N. B. Brookes, G. M. De Luca, M. Salluzzo, T. Schmitt, V. N. Strocov, and G. Ghiringhelli, Phys. Rev. Lett. **104**, 077002 (2010).

[8] M. Le Tacon, G. Ghiringhelli, J. Chaloupka, M. M. Sala, V. Hinkov, M. W. Haverkort, M. Minola, M. Bakr, K. J. Zhou, S. Blanco-Canosa, C. Monney, Y. T. Song, G. L. Sun, C. T. Lin, G. M. De Luca, M. Salluzzo, G. Khaliullin, T. Schmitt, L. Braicovich, and B. Keimer, Nat. Phys. **7**, 725 (2011).

[9] G. Ghiringhelli, M. Le Tacon, M. Minola, S. Blanco-Canosa, C. Mazzoli, N. B. Brookes, G. M. De Luca, A. Frano, D. G. Hawthorn, F. He, T. Loew, M. M. Sala, D. C. Peets, M. Salluzzo, E. Schierle, R. Sutarto, G. A. Sawatzky, E. Weschke, B. Keimer, and L. Braicovich, Science **337**, 821 (2012).

[10] M. P. M. Dean, R. S. Springell, C. Monney, K. J. Zhou, J. Pereiro, I. Božović, B. Dalla Piazza, H. M. Rønnow, E. Morenzoni, J. van den Brink, T. Schmitt, and J. P. Hill, Nat. Mater. **11**, 850 (2012).

[11] M. P. M. Dean, G. Dellea, R. S. Springell, F. Yakhou-Harris, K. Kummer, N. B. Brookes, X. Liu, Y.-J. Sun, J. Strle, T. Schmitt, L. Braicovich, G. Ghiringhelli, I. Božović, and J. P. Hill, Nat. Mater. **12**, 1019 (2013).

[12] M. Dean, J. Magn. Magn. Mater. **376**, 3 (2015).

[13] C. Monney, T. Schmitt, C. E. Matt, J. Mesot, V. N. Strocov, O. J. Lipscombe, S. M. Hayden, and J. Chang, Phys. Rev. B **93**, 075103 (2016).

[14] L. Chaix, E. W. Huang, S. Gerber, X. Lu, C. Jia, Y. Huang, D. E. McNally, Y. Wang, F. H. Vernay, A. Keren, M. Shi, B. Moritz, Z.-X. Shen, T. Schmitt, T. P. Devereaux, and W.-S. Lee, Phys. Rev. B **97**, 155144 (2018).

[15] S. M. Hayden, G. Aeppli, R. Osborn, A. D. Taylor, T. G. Perring, S. W. Cheong, and Z. Fisk, Phys. Rev. Lett. **67**, 3622 (1991).

[16] S. M. Hayden, G. Aeppli, H. A. Mook, T. G. Perring, T. E. Mason, S.-W. Cheong, and Z. Fisk, Phys. Rev. Lett. **76**, 1344 (1996).

[17] M. Arai, T. Nishijima, Y. Endoh, T. Egami, S. Tajima, K. Tomimoto, Y. Shiohara, M. Takahashi, A. Garrett, and S. M. Bennington, Phys. Rev. Lett. **83**, 608 (1999).

[18] P. Dai, H. Mook, S. Hayden, G. Aeppli, T. Perring, R. Hunt, and F. Dogan, Science **284**, 1344 (1999).

[19] R. Coldea, S. M. Hayden, G. Aeppli, T. G. Perring, C. D. Frost, T. E. Mason, S.-W. Cheong, and Z. Fisk, Phys. Rev. Lett. **86**, 5377 (2001).

[20] N. S. Headings, S. M. Hayden, R. Coldea, and T. G. Perring, Phys. Rev. Lett. **105**, 247001 (2010).

[21] O. J. Lipscombe, S. M. Hayden, B. Vignolle, D. F. McMorrow, and T. G. Perring, Phys. Rev. Lett. **99**, 067002 (2007).

[22] A. W. Sandvik and R. R. P. Singh, Phys. Rev. Lett. **86**, 528 (2001).

[23] B. Vignolle, S. M. Hayden, D. F. McMorrow, H. M. Rønnow, B. Lake, C. D. Frost, and T. G. Perring, Nat. Phys. **3**, 163 (2007).

[24] S. Wakimoto, K. Yamada, J. M. Tranquada, C. D. Frost, R. J. Birgeneau, and H. Zhang, Phys. Rev. Lett. **98**, 247003 (2007).

[25] O. J. Lipscombe, B. Vignolle, T. G. Perring, C. D. Frost, and S. M. Hayden, Phys. Rev. Lett. **102**, 167002 (2009).

[26] D. Meyers, H. Miao, A. C. Walters, V. Bisogni, R. S. Springell, M. d'Astuto, M. Dantz, J. Pelliciari, H. Y. Huang, J. Okamoto, D. J. Huang, J. P. Hill, X. He, I. Božović, T. Schmitt, and M. P. M. Dean, Phys. Rev. B **95**, 075139 (2017).

[27] T. P. Croft, C. Lester, M. S. Senn, A. Bombardi, and S. M. Hayden, Phys. Rev. B **89**, 224513 (2014).

[28] L. Braicovich, N. B. Brookes, G. Ghiringhelli, M. Minola, G. Monaco, M. M. Sala, and L. Simonelli, Synchrotron Radiat. News **25**, 9 (2012).

[29] N. B. Brookes, G. Ghiringhelli, P. Glatzel, and M. M. Sala, Synchrotron Radiat. News **31**, 26 (2018).

[30] See https://www.diamond.ac.uk/Instruments/Magnetic-Materials/I21.

[31] L. Braicovich, M. Moretti Sala, L. J. P. Ament, V. Bisogni, M. Minola, G. Balestrino, D. Di Castro, G. M. De Luca, M. Salluzzo, G. Ghiringhelli, and J. van den Brink, Phys. Rev. B **81**, 174533 (2010).

[32] M. M. Sala, V. Bisogni, C. Aruta, G. Balestrino, H. Berger, N. B. Brookes, G. M. de Luca, D. D. Castro, M. Grioni, M. Guarise, P. G. Medaglia, F. M. Granozio, M. Minola, P. Perna, M. Radovic, M. Salluzzo, T. Schmitt, K. J. Zhou, L. Braicovich, and G. Ghiringhelli, New J. Phys. **13**, 043026 (2011).

[33] Y. Y. Peng, E. W. Huang, R. Fumagalli, M. Minola, Y. Wang, X. Sun, Y. Ding, K. Kummer, X. J. Zhou, N. B. Brookes, B. Moritz, L. Braicovich, T. P. Devereaux, and G. Ghiringhelli, Phys. Rev. B **98**, 144507 (2018).

[34] R. Fumagalli, L. Braicovich, M. Minola, Y. Y. Peng, K. Kummer, D. Betto, M. Rossi, E. Lefrancois, C. Morawe, M. Salluzzo, H. Suzuki, F. Yakhou, M. Le Tacon, B. Keimer, N. B. Brookes, M. M. Sala, and G. Ghiringhelli, Phys. Rev. B **99**, 134517 (2019).

[35] M. P. M. Dean, A. J. A. James, R. S. Springell, X. Liu, C. Monney, K. J. Zhou, R. M. Konik, J. S. Wen, Z. J. Xu, G. D. Gu, V. N. Strocov, T. Schmitt, and J. P. Hill, Phys. Rev. Lett. **110**, 147001 (2013).

[36] S. W. Lovesey, *Theory of Neutron Scattering from Condensed Matter* (Clarendon, Oxford, 1986).

[37] L. J. P. Ament, G. Ghiringhelli, M. M. Sala, L. Braicovich, and J. van den Brink, Phys. Rev. Lett. **103**, 117003 (2009).

[38] C. J. Jia, E. A. Nowadnick, K. Wohlfeld, Y. F. Kung, C. C. Chen, S. Johnston, T. Tohyama, B. Moritz, and T. P. Devereaux, Nat. Commun. **5**, 3314 (2014).

[39] J. Lamsal and W. Montfrooij, Phys. Rev. B **93**, 214513 (2016).

[40] P. M. Chaikin and T. C. Lubensky, *Principles of Condensed Matter Physics* (Cambridge University Press, Cambridge, 1995).

[41] L. Chaix, G. Ghiringhelli, Y. Y. Peng, M. Hashimoto, B. Moritz, K. Kummer, N. B. Brookes, Y. He, S. Chen, S. Ishida,

Y. Yoshida, H. Eisaki, M. Salluzzo, L. Braicovich, Z. X. Shen, T. P. Devereaux, and W. S. Lee, Nat. Phys. **13**, 952 (2017).
[42] L. Pintschovius, Phys. Status Solidi B **242**, 30 (2005).
[43] D. Reznik, Physica C **481**, 75 (2012).
[44] T. P. Devereaux, A. M. Shvaika, K. Wu, K. Wohlfeld, C. J. Jia, Y. Wang, B. Moritz, L. Chaix, W.-S. Lee, Z.-X. Shen, G. Ghiringhelli, and L. Braicovich, Phys. Rev. X **6**, 041019 (2016).
[45] See Supplemental Material at http://link.aps.org/supplemental/10.1103/PhysRevB.100.214510 for details of self-absorption calculations [53–56].
[46] D. Scalapino, Phys. Rep. **250**, 329 (1995).
[47] E. W. Huang, D. J. Scalapino, T. A. Maier, B. Moritz, and T. P. Devereaux, Phys. Rev. B **96**, 020503(R) (2017).
[48] A. J. A. James, R. M. Konik, and T. M. Rice, Phys. Rev. B **86**, 100508(R) (2012).
[49] M. V. Eremin, I. M. Shigapov, and H. T. D. Thuy, J. Phys.: Condens. Matter **25**, 345701 (2013).
[50] M. P. M. Dean, A. J. A. James, A. C. Walters, V. Bisogni, I. Jarrige, M. Hücker, E. Giannini, M. Fujita, J. Pelliciari, Y. B. Huang, R. M. Konik, T. Schmitt, and J. P. Hill, Phys. Rev. B **90**, 220506(R) (2014).
[51] A. H. MacDonald, S. M. Girvin, and D. Yoshioka, Phys. Rev. B **41**, 2565 (1990).
[52] B. Dalla Piazza, M. Mourigal, N. B. Christensen, G. J. Nilsen, P. Tregenna-Piggott, T. G. Perring, M. Enderle, D. F. McMorrow, D. A. Ivanov, and H. M. Rønnow, Nat. Phys. **11**, 62 (2015).
[53] R. Comin, R. Sutarto, E. H. da Silva Neto, L. Chauviere, R. Liang, W. N. Hardy, D. A. Bonn, F. He, G. A. Sawatzky, and A. Damascelli, Science **347**, 1335 (2015).
[54] R. Comin, R. Sutarto, F. He, E. H. da Silva Neto, L. Chauviere, A. Fraño, R. Liang, W. N. Hardy, D. A. Bonn, Y. Yoshida, H. Eisaki, A. J. Achkar, D. G. Hawthorn, B. Keimer, G. A. Sawatzky, and A. Damascelli, Nat. Mater. **14**, 796 (2015).
[55] M. Minola, G. Dellea, H. Gretarsson, Y. Y. Peng, Y. Lu, J. Porras, T. Loew, F. Yakhou, N. B. Brookes, Y. B. Huang, J. Pelliciari, T. Schmitt, G. Ghiringhelli, B. Keimer, L. Braicovich, and M. Le Tacon, Phys. Rev. Lett. **114**, 217003 (2015).
[56] A. J. Achkar, F. He, R. Sutarto, C. McMahon, M. Zwiebler, M. Hücker, G. D. Gu, R. Liang, D. A. Bonn, W. N. Hardy, J. Geck, and D. G. Hawthorn, Nat. Mater. **15**, 616 (2016).